JOTCS A
Journal of the Turkish Chemical Society
Section: A
Chemistry
TURKISH CHEMICAL SOCIETY

Structural Properties, Photoluminescence, and Judd-Ofelt Parameters of Eu^{3+}- Doped $CoNb_2O_6$ Phosphor

Mustafa İlhan*[a], Lütfiye Feray Güleryüz[b], Mete Kaan Ekmekçi[c]

[a*]Department of Environmental Engineering, Faculty of Engineering, Marmara University, Maltepe, 34854, İstanbul, Türkiye
[b]Department of Mechanical Engineering, Faculty of Engineering, Ege University, Bornova, 35040, İzmir, Türkiye
[c]Marmara University, Department of Chemistry, Faculty of Science, Marmara University, Kadıköy, 34722, Istanbul, Türkiye

Abstract: Trivalent Eu-activated $CoNb_2O_6$ phosphors were fabricated using the molten salt method, which provides enhanced homogeneity and low sintering temperature. The ceramic samples were examined by spectral and structural analyses. In X-ray diffractions, the single phase of orthorhombic columbite type $CoNb_2O_6$ structure was obtained for 0.5-10 mol% Eu^{3+} doping concentrations, while a two theta peak shift towards the smaller angles occurred. SEM examinations show an irregular morphology and sub-micron grain sizes. In photoluminescence (PL) spectra, the phosphors showed typical Eu^{3+} emissions with the $^5F_0 \rightarrow {}^7F_J$ (J=0, 1, 2, 3, 4) transitions, and high emission peaks were observed at the $^5D_0 \rightarrow {}^7F_2$ transition. The photoluminescence of $CoNb_2O_6$:Eu^{3+} decreased over 5 mol% because of the concentration quenching. The energy transfer mechanism and critical distance of the phosphor are the dipole-dipole (d–d) interaction, and 15.70 Å, respectively. The spectral features of the phosphors were assessed by calculating the Judd-Ofelt intensity parameters (Ω_2, Ω_4) from the PL emission spectrum. The low Ω_2 parameter values or/and the $\Omega_4 > \Omega_2$ trend for $CoNb_2O_6$:Eu^{3+} phosphors were related to the less covalent or more ionic character of the Eu^{3+}–O^{2-} bond and the high local symmetry of the Eu^{3+} sites, while the high Ω_4 parameter values may be ascribed to the decrease in the electron density in the ligands.

Keywords: $CoNb_2O_6$; XRD; Eu^{3+} doping; photoluminescence; Judd-Ofelt analysis.

Submitted: May 08, 2023. **Accepted:** June 23, 2023.

Cite this: İlhan M, Güleryüz LF, Ekmekçi MK. Structural Properties, Photoluminescence, and Judd-Ofelt Parameters of Eu3+- Doped CoNb2O6 Phosphor. JOTCSA. 2023;10(3):745–56.

DOI: https://doi.org/10.18596/jotcsa.1294230.

***Corresponding author. E-mail:** mustafa.ilhan@marmara.edu.tr.

1. INTRODUCTION

Rare earth (RE) ions with 4f–4f inner shell transitions have undoubtedly contributed in a great manner to the development of luminescent applications and the increase in their use. Therefore, the RE ion-activated phosphors lead to numerous innovations in the development of new generation devices in various fields such as screen-display technology, lighting technology, and optical data communication due to some positive features such as long life, energy saving, improved physical durability, fast switching, small size, environmental friendliness, and high efficiency (1-16). The trivalent europium ion (Eu^{3+}) is known for its strong luminescence in the red spectral region, which exhibits interesting spectral properties, as well as having non-degenerate (J=0) first levels of transitions in both the absorption and luminescence spectrum and has a great advantage over other RE ions (10-14). The trivalent europium ion has $^5D_0 \rightarrow {}^7F_J$ (J=0, 1, 2, 3, 4, 5, 6) transitions. Among the transitions, $^5D_0 \rightarrow {}^7F_2$ is electric dipole (hypersensitive transition) and its intensity very strongly dependent

on environment, while the $^5D_0 \rightarrow {}^7F_1$ transition is magnetic dipole and intensity largely independent of environment (12-14).

The columbite-type structured divalent metal-niobium oxide compounds with orthorhombic symmetry can be formulated as MNb_2O_6 (M= Co, Mg, Sr, Mn, Ni, Cd, etc). The MNb_2O_6 structure has a significant benefit in that it can host guest ions that have ionic sizes comparable to those of the Nb and divalent M^{2+} ions present in the structure. As MNb_2O_6 structure, cobalt niobate ($CoNb_2O_6$) compound consisting of the CoO_6-NbO_6 octahedral (15-18) has been studied due to its magnetic (19-22), neutron scattering (23), dielectric (24), optical (25-27), gas sensing (28,29) magnetic-thermodynamic (29,30) properties. MNb_2O_6 (M= Ni, Zn, Co) sensing electrodes (SEs) were produced and studied for NO_2 detection at high temperature where $CoNb_2O_6$ electrode has the highest sensibility at 750 °C among the oxide SEs (29). The transitions of magnetic phase for $CoNb_2O_6$ were studied by measuring the specific heat, magnetic phase diagram, and magnetic susceptibility at 2.9 and 1.9 K (30). The low-temperature heat capacity and spin entropy properties of $CoNb_2O_6$ have been investigated (31). The molten salt method is one of the favorite synthetic methods used in the synthesis of niobates due to its advantageous properties such as short reaction time, low sintering temperature, improved homogeneity, and crystallinity (15, 18, 25-27). The superiority of the molten salt method may be assessed by comparison of the conventional solid-state method. The fabrication of $CoNb_2O_6$ by solid state reaction has been reported by different researchers as 900 (32), 900-1300 (24), and 1400 °C (33) as sintering temperatures and sintering times as 72, 6, and 22 h, respectively. Besides, $CoNb_2O_6$ has produced by the molten salt method at 800 °C for 4 h period (25-27).

In the study, the structural, photoluminescence properties and Judd-Ofelt intensity parameters of $Co_{1-x}Nb_2O_6$:xEu^{3+} (x=0.5, 1.5, 3, 5, 7, and 10 mol%) phosphors were studied. The spectroscopic and structural analyses of the samples were performed by XRD, SEM-EDS and PL.

2. EXPERIMENTAL

The $Co_{1-x}Nb_2O_6$:xEu^{3+} (x=0.005, 0.015, 0.03, 0.05, 0.07, 0.1 or x=0.5, 1.5, 3, 5, 7, 10 mol%) powders were fabricated by the molten salt route. In the synthesis, cobalt nitrate hexahydrate ($Co(NO_3)_2.6H_2O$) (Sigma-Aldrich, 98.5%), niobium oxide (Nb_2O_5) (Alpha Aesar, 99.9%), and europium oxide (Eu_2O_3) (Alpha Aesar, 99.9%) were used. For the synthesis, Li_2SO_4/Na_2SO_4 (salt/salt), and $Li_2SO_4+Na_2SO_4/CoO+Nb_2O_5+Eu_2O_3$ (salt/oxide) molar ratio were taken as 0.635/0.365 and 2/1 weight ratio, respectively. The oxide mixtures and salt mixtures were prepared according to their stoichiometric ratios and mixed well in an agate mortar to provide homogeneity. The resulting mixtures were subsquently placed in an alumina crucible and sintered for 15 h at 800 °C in air atmosphere using an electric furnace. After the sintering, the phosphor powders were washed down several times with bi-distilled water to get rid of the ionic salts and filtered using a vacuum pump several times. The remnants of Cl^- ions in the solution were controlled by qualitative analysis.

The phase structure of the ceramics was investigated by X-ray diffraction (XRD), (D2 PHASER, Bruker Corp., Germany) using Cu-K$_\alpha$ radiation, Ni filter, scan rate = 2 °/min, 2θ=20-65°. The grain morphology and elemental identification were examined by scanning electron microscopy (SEM) (JSM-5910LV, JEOL Ltd., Japan) equipped with energy dispersive spectroscopy (EDS) (INCAx-Sight 7274, Oxford Industries, UK) after Au coating. PL (photoluminescence) results were obtained using fluorescence spectrometer (FLS920, Edinburgh Inst., UK) with a 450 W xenon lamp.

3. RESULTS AND DISCUSSION

3.1. XRD and SEM-EDS Results

Figure 1 presents the X-ray diffraction patterns of Eu^{3+}-doped $CoNb_2O_6$ samples. XRD results of the ceramic samples was defined by orthorhombic columbite symmetry (JCPDS no: 32-0304) with space group *Pbcn*60. As seen in Figure 1, there is no secondary or a minor phase in the XRD patterns of Eu^{3+}-doped $CoNb_2O_6$ samples, which may be attributed to the successful incorporation of Eu^{3+} ions into the columbite structure. The cell parameters of orthorhombic $CoNb_2O_6$ are a=14.167 Å, b=5.714 Å, c=5.046 Å, and V=408.47 Å^3 (30). The schematic representation of the $CoNb_2O_6$ crystalline structure consisting of corner-shared and edge-shared NbO_6 and CoO_6 octahedra is shown in Figure 2. Based on the ionic radius and coordination number (CN), the formation of the single-phase may be attributed to the substitution of Eu^{3+} ions with ionic radius 0.947 Å (for 6 C.N) by Co^{2+} ions (r=0.745 Å, for C.N. 6). The XRD peaks of the (131) reflection are shown in Figure 3. There are shifts towards smaller two-theta angles of the (131) XRD peak with the increase of Eu^{3+} concentration. Accordingly, the expansion of the lattice due to the large ionic radius of the Eu^{3+} ion, where the Eu^{3+} substitution instead of Co^{2+} is also likely to affect the charge balance and form some stress in the structure. However, despite some expansion in the lattice volume, the existence of the single-phase structure was preserved up to 10 mol% concentration, indicating that the dopant ion has located into the structure successfully.

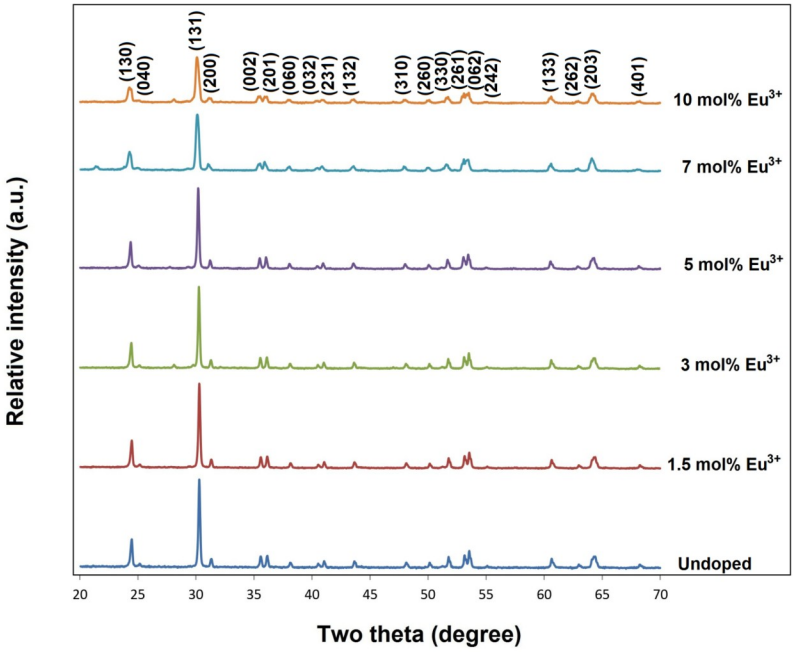

Figure 1: X-ray diffraction results of undoped and 0.5, 1.5, 3, 5, 7, and 10 mol% Eu^{3+} doped samples.

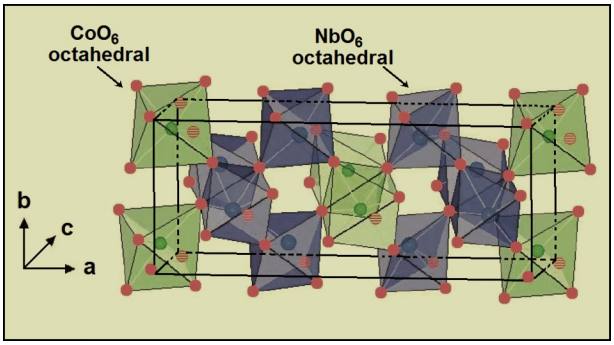

Figure 2: Schematic illustration of the $CoNb_2O_6$ crystal structure.

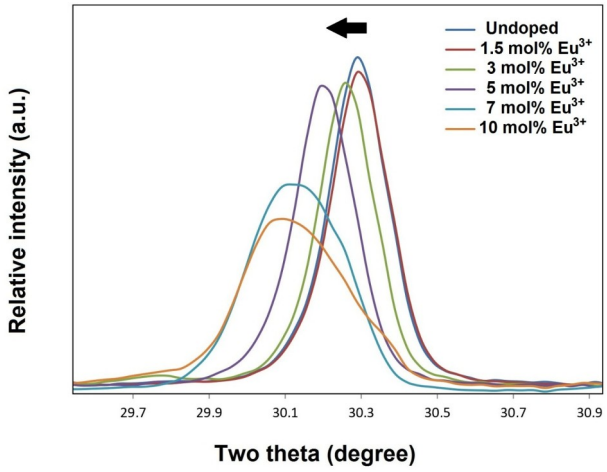

Figure 3: XRD two theta angles (131) shifted to lower angles with Eu^{3+} concentration.

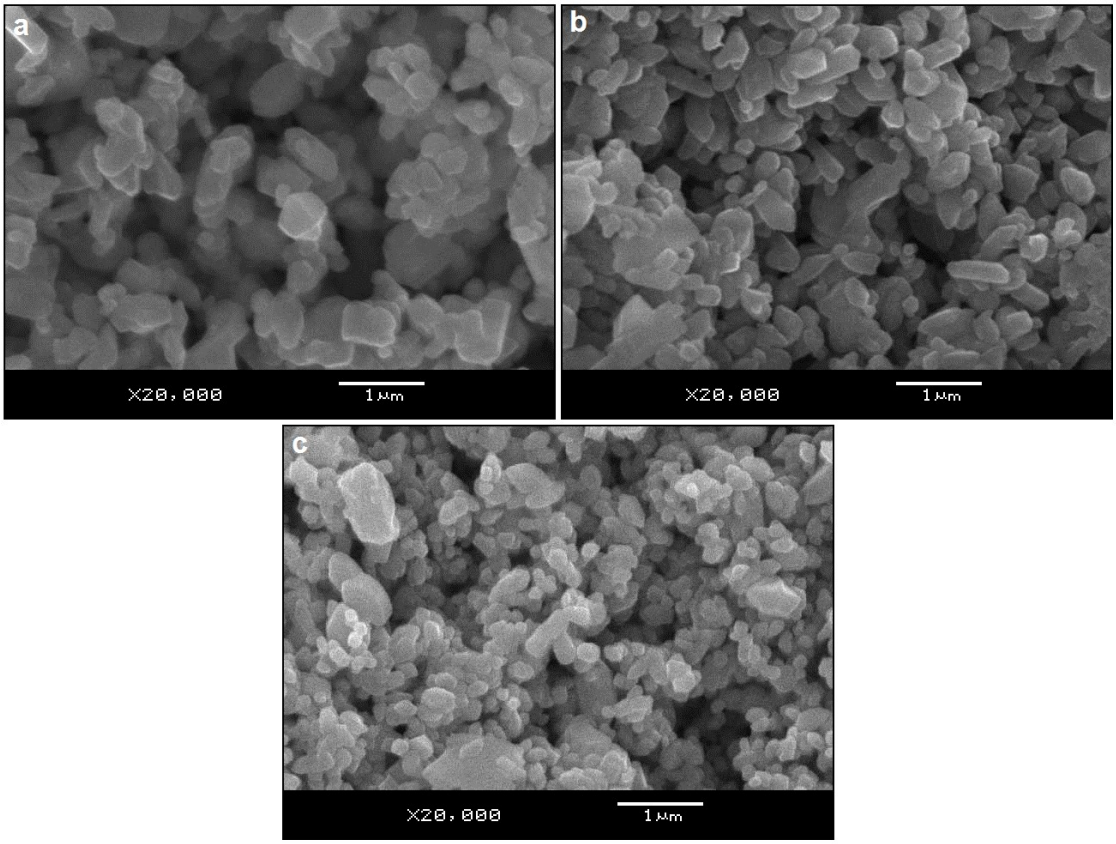

Figure 4: SEM micrographs of (a) undoped, (b) 5, (c) 10 mol% Eu^{3+} doped samples at 20000× magnifications and 20 kV acceleration voltage.

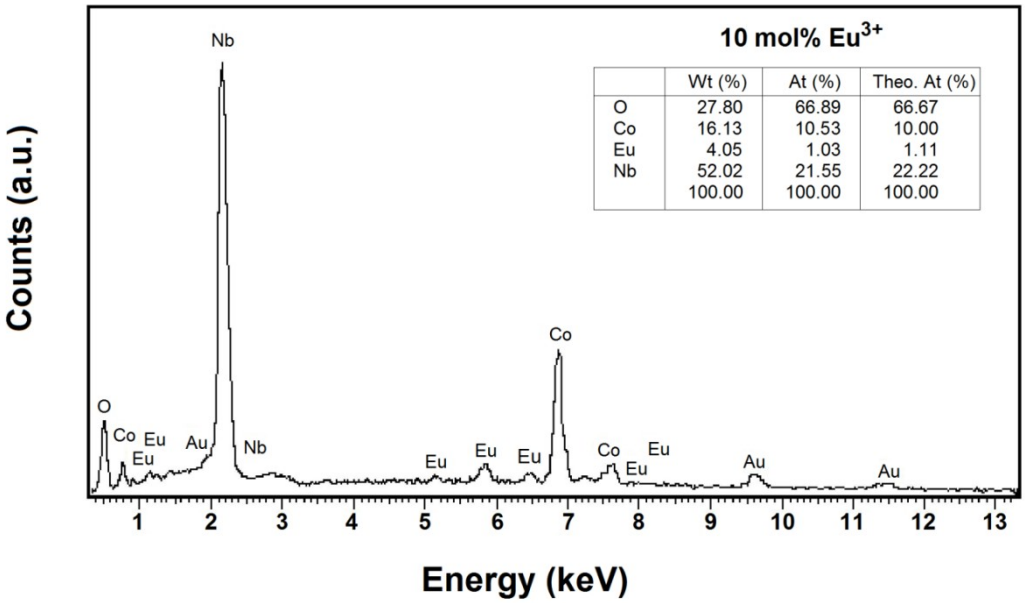

	Wt (%)	At (%)	Theo. At (%)
O	27.80	66.89	66.67
Co	16.13	10.53	10.00
Eu	4.05	1.03	1.11
Nb	52.02	21.55	22.22
	100.00	100.00	100.00

Figure 5: EDS spectrum and wt%, at% elemental compositions, and theoretical at% values for 10 mol% Eu^{3+}-doped sample.

Figure 4(a-c) shows the SEM micrographs at 20000x magnification for undoped $CoNb_2O_6$, 5, and 10 mol% Eu^{3+} doped samples, respectively. As seen in the SEM micrographs, the morphology of the grains was affected by the Eu^{3+} concentration. The grain shapes of the Eu^{3+} doped samples had a roundish, angular and irregular morphology, while the grain sizes, mostly in submicron scale, ranged from 0.05 to 2 µm. As seen from the SEM micrographs, the grain size reduced slightly as the concentration increases. The reason for the decrease in grain size with an increase in Eu^{3+} concentration could be attributed to the suppression of grain growth due to lattice restriction (15,34). Figure 5 shows the elemental compositions for the sample of $CoNb_2O_6$ doped with 10 mol% Eu^{3+} obtained using EDS, as weight (%) and atomic (%), by applying SEM acceleration voltage of 20 kV. According to the EDS results, the atomic compositions (%) and theoretical atomic compositions (%) of O, Co, Eu, Nb elements are 66.89, 10.53, 1.03, 21.55 and 66.67, 10.00, 1.11, 22.22, respectively, where the elemental compositions of Eu^{3+} doped $CoNb_2O_6$ agree with the theoretical compositions.

3.2. Photoluminescence of $CoNb_2O_6$:Eu^{3+}

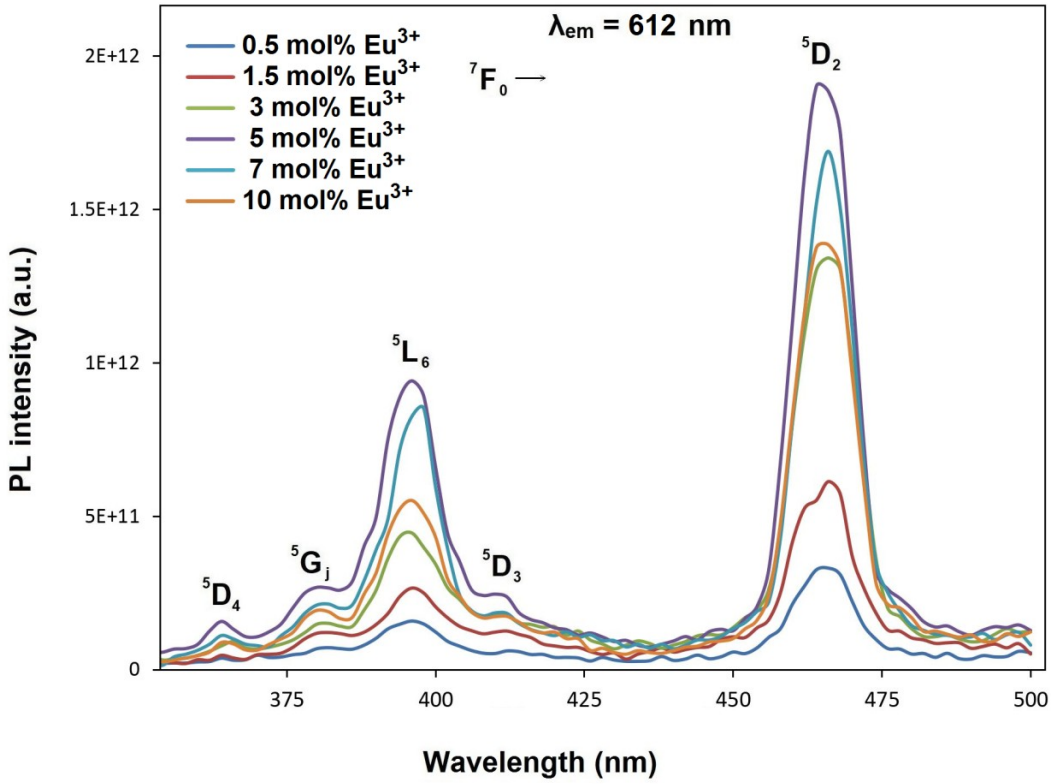

Figure 6: PL excitation spectra of the 0.5-10 mol% range of Eu^{3+} doped $CoNb_2O_6$ phosphors under 612 nm emission.

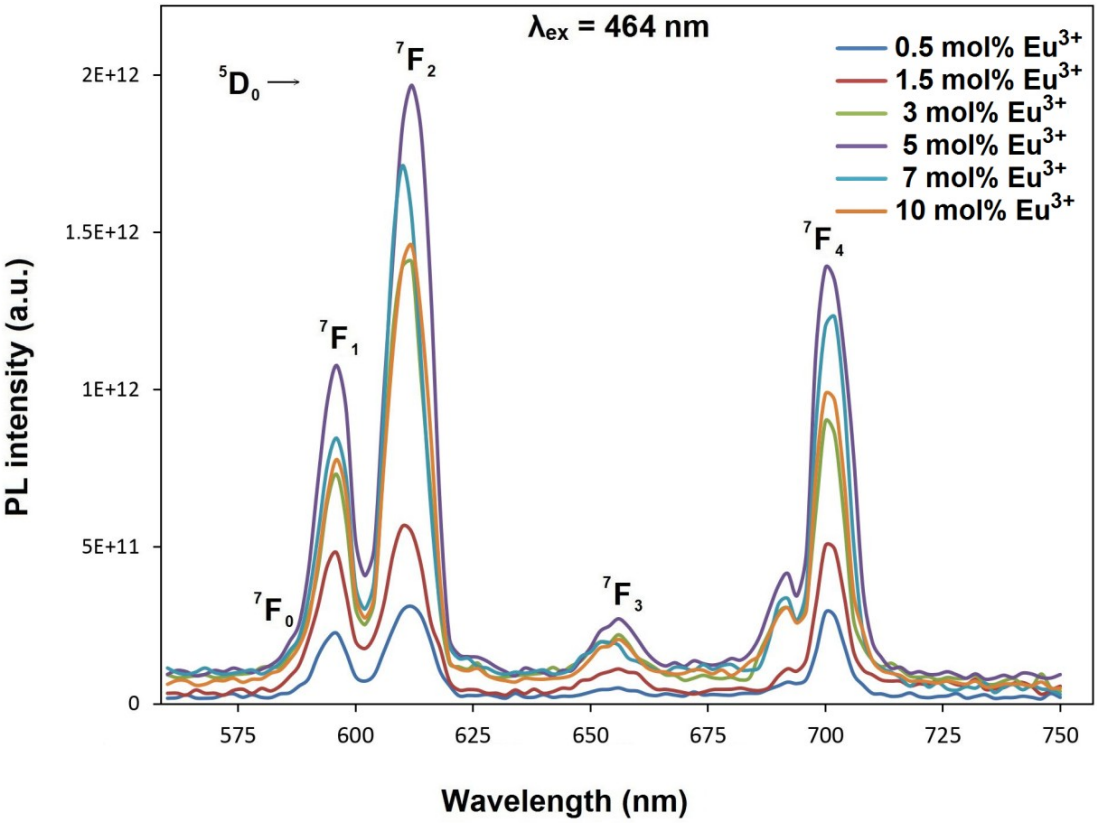

Figure 7: PL emission spectra of the 0.5-10 mol% range of Eu^{3+}-doped $CoNb_2O_6$ phosphors with the excitation of 464 nm.

Figure 6 shows the PL excitations of $CoNb_2O_6$:Eu^{3+} phosphors were recorded at emission wavelength of 612.0 nm, where the PL excitations were assigned with transitions of $^7F_0 \rightarrow {}^5D_4$, $^7F_0 \rightarrow {}^5G_J$, $^7F_0 \rightarrow {}^5L_6$, $^7F_0 \rightarrow {}^5D_3$, and $^7F_0 \rightarrow {}^5D_2$. The PL emissions of $CoNb_2O_6$:Eu^{3+} phosphors were monitored at the $^5D_0 \rightarrow {}^7F_0$, $^5D_0 \rightarrow {}^7F_1$, $^5D_0 \rightarrow {}^7F_2$, $^5D_0 \rightarrow {}^7F_3$, $^5D_0 \rightarrow {}^7F_4$ transitions with the excitation of 464 nm are shown in Figure 7. In all samples, the emission intensities of the $^5D_0 \rightarrow {}^7F_2$ (electric dipole) transition are higher than the $^5D_0 \rightarrow {}^7F_1$ (magnetic dipole) transition, which indicates Eu^{3+} ions occupying crystallographic sites without an inversion center (34,35). As given in Figure 7, the phosphor's PL emission increased by increasing concentration to 5 mol%, but decreased at 7 and 10 mol% due to concentration quenching. As the concentration of Eu^{3+} increases, the distance between Eu^{3+} ions decreases and non-radiative energy transfer becomes more significant. Accordingly, when the concentration of dopant ion reached the critical level, the critical distance (R_c) will be important for concentration quenching which promotes non-radiative energy transfer. The critical distance (R_c) for the energy transfer between Eu^{3+}-Eu^{3+} ions can be found by Eq. (1) (36):

$$R_C \approx 2\left(\frac{3V}{4\pi X c N}\right)^{1/3} \quad (1)$$

where V represents the volume of a unit cell, N (or Z) denotes the quantity of sites where a dopant ion can be placed, and X_c is the minimum concentration required for the dopant ion to be effective. For $CoNb_2O_6$:Eu^{3+} phosphor, it is X_c =0.05 mol ion in the unit cell, V=408.47 Å^3 (30), and N=4. The critical distance (R_c) between Eu^{3+}–Eu^{3+} ions for energy transfer was calculated as 15.70 Å. According to Blasse's theory (37), if the distance between Eu^{3+}–Eu^{3+} ions is greater than 5 Å, the effective mechanism for energy transfer will be multipolar interaction, while the mechanism of exchange interaction will not be effective. The interaction type of energy transfer mechanism can be estimated by Van Uitert's theory (38). The theory suggests that if energy transfer occurs between dopants of the same type, Eq. (2) can be used to determine the

type of multipolar interaction mechanism, based on changes in emission intensity and ion concentration:

$$\frac{I}{x}=K\left[1+\beta(x)^{\Theta/3}\right]^{-1} \tag{2}$$

where the character of the multipolar interaction is represented by θ, while the RE concentration is represented by x. The ratio of emission intensity (I) to phosphor concentration (x) is represented by I/x. The constants K and β belong to the phosphor and are measured at the same excitation wavelength. The values of θ=6, θ=8, and θ=10 represent dipole–dipole (d–d), dipole–quadrupole (d–q), and quadrupole–quadrupole (q–q) interactions, respectively. If $\beta(x)^{\theta/3} \gg 1$ is accepted, Eq. (2) can be modified into Eq. (3):

$$\log(I/x)=K'-\Theta/3\log x\,(K'=\log K-\log\beta) \tag{3}$$

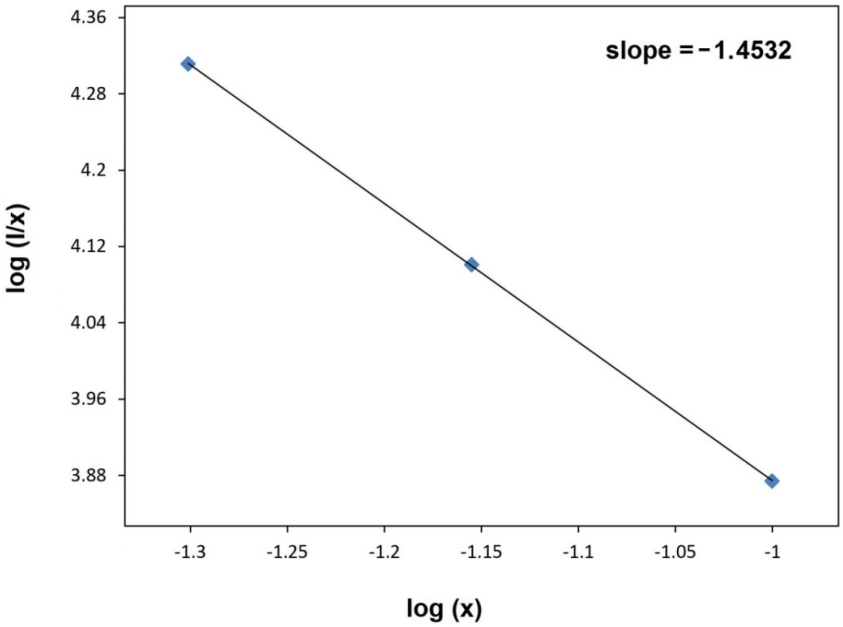

Figure 8: Relation between the $\log_{10}(I/x)$ and $\log_{10}(x)$ of $CoNb_2O_6:Eu^{3+}$ phosphors.

The θ parameter can be estimated from the slope of equation (3) which is plotted between the log (I/x) and log (x). The graph of log (I/x) as a function of log (x) for $CoNb_2O_6:Eu^{3+}$ phosphors is given in Figure 8. The critical concentration of Eu^{3+} was taken as $x \geq 0.05$. This plot shows the dependence of log (I/x) on log (x) of Eu^{3+} where the estimated value of the slope is about -1.4532. The θ value was determined as 4.36, which is close to 6. Correspondingly, the energy transfer mechanism of the phosphor can be ascribed to the dipole-dipole (d–d) interaction.

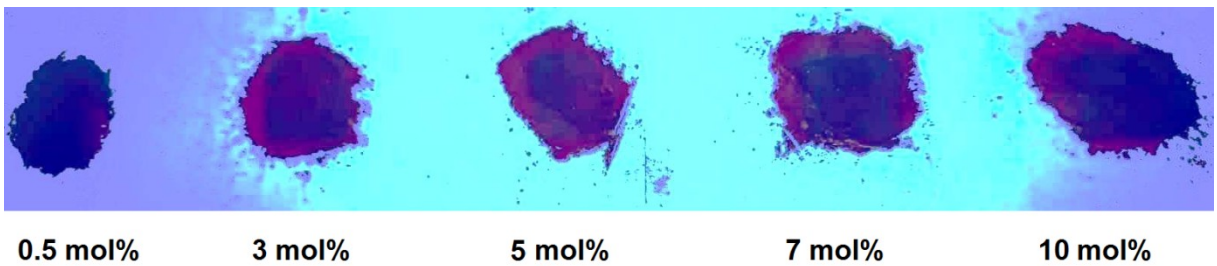

Figure 9: UV lamp photos of $CoNb_2O_6:xEu^{3+}$ (x=0.5, 3, 5, 7, 10) phosphors at 365 nm.

The UV lamp photographs of the phosphors under 365 nm are given in Figure 9. As seen from the pictures, the Eu^{3+}-doped phosphors have pale purple color, while the brightness slightly increased depending on the Eu^{3+} concentration.

Judd-Ofelt analysis and radiative properties

JO (Judd-Ofelt) intensity parameters are important in assessing the effectiveness of luminescent materials (39,40). The Eu^{3+} has distinctive properties among the RE^{3+} ions in determining JO intensity parameters because of its magnetic dipole transition ($^5D_0 \rightarrow {}^7F_1$), which is not affected by the surrounding environment and can serve as a standard for transitions originating from the $^5D_0$ level. By utilizing the emission spectra of materials containing Eu^{3+}, JO intensity parameters Ω_J (J=2,4,6) can be calculated using Eq. (4) (41,42):

$$\Omega_J = \frac{S_{MD}(V_1^3)}{e^2 V_J^3} \frac{9n^3}{n(n^2+2)^2} \frac{\int I_1(V_1)}{|\langle J \| U^J \| J' \rangle|^2 \int I_J(V_J)} \tag{4}$$

where the transition frequencies V_1, V_J and the integrated intensities I_1, I_J correspond to the $^5D_0 \rightarrow {}^7F_1$ and $^5D_0 \rightarrow {}^7F_J$ transitions, respectively. The magnetic dipole line strength is $S_{MD}=9.6 \cdot 10^{-42}$ (esu^2cm^2), and the refractive index is denoted by n. The elementary charge e is equal to $4.803 \cdot 10^{-10}$ (esu). The total angular momenta of the initial and final states are represented by J and J', respectively. The double reduced matrix elements for unit tensor operators are expressed as $|\langle J||U^J||J'\rangle|^2$. Only the $^5D_0 \rightarrow {}^7F_2$ (U^2=0.0032), $^5D_0 \rightarrow {}^7F_4$ (U^4=0.0023), and $^5D_0 \rightarrow {}^7F_6$ (U^6=0.0002) transitions have non-zero reduced matrix elements for all electric dipole (ED) transitions originating from the $^5D_0$ level (35).

The radiative transition probabilities are determined using the $^5D_0 \rightarrow {}^7F_J$ (J=1, 2, 4, 6) transitions, while the $^5D_0 \rightarrow {}^7F_J$ (J=0, 3, 5) transitions are not allowed and are therefore excluded from the JO calculation. Although the Ω_6 parameter is related to the $^5D_0 \rightarrow {}^7F_6$ transition, it was not incorporated in the calculation due to its inability to be detected by PL in the infrared region. Nonetheless, this transition's impact on the calculation is insignificant, as some studies have reported (18,41). The dipole strength determines the spontaneous transition probability (A), which can be expressed using Eq. (5):

$$A(J, J') = \frac{64\pi^4 V^3}{3h(2J+1)} [X_{ED} S_{ED} + X_{MD} S_{MD}] \tag{5}$$

where S_{ED} and S_{MD} are line strengths of electric and magnetic dipole moments respectively, and are expressed as esu^2cm^2 units. Planck's constant is denoted by "h". The formula for calculating the electric dipole line strengths (S_{ED}) based on the JO parameters is given by Eq. (6):

$$S_{ED}(J, J') = e^2 \sum_{J=2,4,6} \Omega_J \times |\langle J || U^J || J' \rangle|^2 \tag{6}$$

The local field corrections for the ED and MD transitions are represented by the χ_{ED} and χ_{MD}, which can be obtained using Eq. (7) and Eq. (8) correspondingly:

$$X_{ED} = \frac{n(n^2+2)^2}{9} \tag{7}$$

$$X_{MD} = n^3 \tag{8}$$

$$\frac{n^2-1}{n^2+2} \times \frac{1}{\rho} = \frac{\sum l_i r_i}{M} \tag{9}$$

where n is the refractive index. The n value for $CoNb_2O_6$ can be estimated from the Lorenz-Lorentz formula Eq. (9) (42-45):

where the compound's molar mass (M), density (□), and specific refraction (r_i) were used to determine its refraction index (n) value, while l_i represents the atomic number of the element in the compound's nominal chemical formula. For $CoNb_2O_6$, the refraction index was found to be 1.974. Table 1 shows the Judd-Ofelt intensity parameters (Ω_2, Ω_4). The Ω_2 parameter is related to the hypersensitive $^5D_0 \rightarrow {}^7F_2$ electric dipole transition, which indicates the covalency of the Eu-O bond and the changes in the Eu^{3+} ion's environment. The Ω_4 parameter is associated with the electron density of the neighboring ligands, and the higher values of Ω_4 parameter indicate lower electron density. The Ω_2 parameter reflects short-range effects, whereas the Ω_4 parameter reflects long-range effects (46, 47). In Table 1, the Ω_2 and Ω_4 parameters are in the range of 2.547-4.242 and 4.504-6.297, respectively. The low Ω_2 parameter values or/and the $\Omega_4 > \Omega_2$ trend are considered as a decrease in the Eu^{3+}-O^{2-} covalent bond and the high local symmetry of the Eu^{3+} sites, where the nature of the Eu^{3+}–O^{2-} bond is less covalent or more ionic. Additionally, the high values of Ω_4 parameter may be attributed to a decrease in electron density in the ligands.

Table 1 J-O parameters (Ω_2, Ω_4), radiative transition and total transition probabilities ($A(J,J')$, (A_r)), branching ratios ((β_{cal}), (β_{exp})), and branching ratio differences (%) of $CoNb_2O_6$:Eu^{3+} phosphor.

Eu^{3+} conc. (mol%)	Eu^{3+} transitions	Ω_2 (10^{-20} cm^2)	Ω_4 (10^{-20} cm^2)	$A(J,J')$ (s^{-1})	A_r (s^{-1})	β_{cal} (%)	β_{exp} (%)	Difference (%)
0.5	$^5D_0 \rightarrow {}^7F_1$	2.878	5.118	92.081	424.436	21.70	23.23	6.61
	$^5D_0 \rightarrow {}^7F_2$			179.116		42.20	43.91	3.89
	$^5D_0 \rightarrow {}^7F_4$			153.239		36.10	32.86	8.98
1.5	$^5D_0 \rightarrow {}^7F_1$	2.547	4.504	91.845	385.917	23.80	25.40	6.29
	$^5D_0 \rightarrow {}^7F_2$			159.150		41.24	42.86	3.77
	$^5D_0 \rightarrow {}^7F_4$			134.923		34.96	31.74	9.20
3	$^5D_0 \rightarrow {}^7F_1$	4.015	4.909	91.660	488.782	18.75	19.98	6.13
	$^5D_0 \rightarrow {}^7F_2$			250.146		51.18	52.86	3.19
	$^5D_0 \rightarrow {}^7F_4$			146.976		30.07	27.16	9.67
5	$^5D_0 \rightarrow {}^7F_1$	3.522	5.219	91.905	468.080	19.63	20.94	6.24
	$^5D_0 \rightarrow {}^7F_2$			219.757		46.95	48.73	3.66
	$^5D_0 \rightarrow {}^7F_4$			156.418		33.42	30.33	9.25
7	$^5D_0 \rightarrow {}^7F_1$	4.242	6.297	91.886	544.752	16.87	18.03	6.47
	$^5D_0 \rightarrow {}^7F_2$			265.035		48.65	50.65	3.94
	$^5D_0 \rightarrow {}^7F_4$			187.831		34.48	31.32	9.17
10	$^5D_0 \rightarrow {}^7F_1$	3.816	5.395	91.840	491.815	18.67	19.91	6.20
	$^5D_0 \rightarrow {}^7F_2$			238.079		48.41	50.23	3.63
	$^5D_0 \rightarrow {}^7F_4$			161.896		32.92	29.86	9.29

Table 1 presents the radiative transition probabilities ($A(J,J')$), total radiative transition probabilities ($\Sigma A(J,J')$ or A_r), and branching ratios (β_{cal}) for the JO intensity parameters. The branching ratio (β or β_{cal}) of the Judd-Ofelt theory can be obtained using Eq. (10) (41,47) from the radiative transition probability ($A(J,J')$) and total radiative transition probability ($\Sigma A(J,J')$):

$$\beta(\%) = \frac{A(J,J')}{\sum A(J,J')} \cdot 100\,\% \tag{10}$$

The values of branching ratio (β>50%) are associated with the potential of laser emission (41,47). However, the branching ratios (β_{cal}) of $^5D_0 \rightarrow {}^7F_2$ transition for $CoNb_2O_6$:Eu^{3+} were found to be between 41.24-51.18% and slightly below 50%. The experimental branching ratios (β_{exp}) obtained from the emission spectrum can be used to evaluate the branching ratios (β_{cal}) of Judd-Ofelt theory. On the other hand, this theory typically has an inherent error of approximately 15%, on describing spectral intensities (41,48). The variations between the experimental (β_{exp}) and calculated values (β_{cal}) of all

phosphors were determined to be between 3.19-9.67%, as shown in Table 1, which are less than 15%. In addition, the radiative lifetime found based on the JO parameterization is comparable to the theoretical lifetime value, which is obtained from the Eu^{3+} emission spectrum, and can be determined via Eq. (11) (48):

$$\tau th = \frac{n_1^3}{14.65} \frac{I_1}{I_{tot}} \tag{11}$$

where the $^5D_0 \rightarrow {}^7F_1$ transition's integrated intensity is represented by I_1, the refractive index is represented by n, and I_{tot} represents the total integrated intensity. Table 2 displays the tabulated values for both the radiative lifetime (τ) and the theoretical radiative lifetime (τ_{th}). The τ and τ_{th} values of $CoNb_2O_6$:Eu^{3+} phosphors from 0.5 to 10 mol% Eu^{3+} varied between 2356-2033 μs and 2217-1925 μs, respectively, and the compatibility of radiative lifetimes was found in the range of 91.37-97.24%.

Table 2: Comparison of radiative lifetimes calculated according to JO parameters and Eq. (11).

Eu^{3+} conc. (mol%)	τ_{exp} (μs)	τ_{th} (μs)	Compatibility (%)
0.5	2356	2217	94.12
1.5	2591	2368	91.37
3	2046	1953	95.44
5	2136	2034	95.21
7	1836	1785	97.24
10	2033	1925	94.66

4. CONCLUSION

The structural, spectral properties and Judd-Ofelt parameterization of Eu^{3+} doped $CoNb_2O_6$ phosphors fabricated by the molten salt synthesis route were investigated in the study. In XRD results, the single-phase orthorhombic columbite structure of Eu^{3+} doped $CoNb_2O_6$ was determined between 0.5 and 10 mol% concentrations. SEM micrographs of the grains showed irregular morphology and the grain sizes varied from 0.05 to 2 ⌣m. EDS results indicated that the elemental compositions of Eu^{3+}-doped $CoNb_2O_6$ agree with the theoretical compositions. The phosphors displayed Eu^{3+} emissions with $^5F_0 \rightarrow {}^7F_J$ (J=0, 1, 2, 3, 4) transitions, and showed dominant peaks at the $^5D_0 \rightarrow {}^7F_2$ transition in PL spectra. Concentration quenching caused a decrease in the PL emissions of $CoNb_2O_6$:Eu^{3+} over 5 mol%. The critical distance and energy transfer mechanism of the phosphor were determined to be 15.70 Å and dipole-dipole (d–d) interaction, respectively. The Judd-Ofelt intensity parameters (Ω_2, Ω_4) were calculated from the PL emission spectrum to evaluate the spectral properties of the phosphors. The high Ω_4 parameter values or/and the $\Omega_4 > \Omega_2$ trend for the phosphors were explained by the high local symmetry of the Eu^{3+} ion, in which the Eu^{3+}–O^{2-} bond has the less covalent or more ionic character. The high values of the Ω_4 parameter was associated with the decrease in electron density in the ligands. The differences of the experimental and calculated branching ratios of all phosphors were estimated between 3.19-9.67%, which is below 15%.

5. CONFLICT OF INTEREST

There is no conflict of interest.

6. REFERENCES

1. Lohan R, Kumar A, Sahu MK, Mor A, Kumar V, Deopa N, Rao AS. Structural, thermal, and luminescence kinetics of $Sr_4Nb_2O_9$ phosphor doped with Dy^{3+} ions for cool w-LED applications. J. Mater. Sci: Mater. Electron 2023;34:694. Available from: <URL>.

2. Kanmani GV, Ponnusamy V, Rajkumar G, Kennedy SMM. A new Eu^{3+}-activated milarite-type potassium magnesium zinc silicate red-emitting phosphor for forensic applications. J. Mater Sci:

Mater Electron 2023;34:765. Available from: <DOI>.

3. Swathi BN, Krushna BRR, Manjunatha K, Wu SY, Subramanian B, Prasad BD, Nagabhushana H. Single phased vivid red-emitting $CaLa_2ZnO_5:Eu^{3+}$ nanophosphor: WLEDs, visualization of latent fingerprints and anti-counterfeiting applications, Mater. Res. Bull. 2023;165:112279. Available from: <DOI>.

4. Ekmekçi MK, İlhan M, Başak AS, Deniz S. Structural and luminescence properties of Sm^{3+} doped TTB-type $BaTa_2O_6$ ceramic phosphors. J. Fluoresc. 2015;25:1757–1762. Available from: <DOI>.

5. Güleryüz LF. Effect of Nd^{3+} doping on structural, near-Infrared, and cathodoluminescent properties for cadmium tantalate phosphors. JOTCSA. 2023;10:77–88. Available from: <DOI>.

6. Hajlaoui T, Pinsard M, Kalhori H, Légaré F, Pignolet A. Second harmonic generation in ferroelectric $Ba_2EuFeNb_4O_{15}$-based epitaxial thin films. Opt. Mater. Express 2020;10: 1323–1334. Available from: <DOI>.

7. İlhan M, Keskin İÇ. Evaluation of the Structural, near-infrared luminescence, and radioluminescence properties of Nd^{3+} activated TTB-lead metatantalate phosphors. JOTCSA. 2023;10:453–66. Available from: <DOI>.

8. Sheikh S, Hussain F. Structural, Dielectric, and Magnetic Properties of Ba_2Bi_{9-xFe5} $+xTi_8O_{39}$ tetragonal tungsten bronze ceramics. Mater. Res. Express 2023;10:036103. Available from: <DOI>.

9. İlhan M, Güleryüz LF. Cathodoluminescence and photoluminescence of $BaTa_2O_6:Sm^{3+}$ phosphor depending on the sintering temperature. Chem. Pap. 2022;76:6963-6974. Available from: <DOI>.

10. Shrivastava R, Khaparde S. Luminescence studies of diopside doped with various concentrations of Dysprosium (III). Res. Chem. Intermed. 2022;48:969-982. Available from: <DOI>.

11. Li J, Wang X, Cui R, Deng C. Synthesis and photoluminescence studies of novel double-perovskite phosphors, Ba_2GdTaO_6: Eu^{3+} for WLEDs. Optik 2020;201:163536. Available from: <DOI>.

12. İlhan M, Güleryüz LF. Boron doping effect on the structural, spectral properties and charge transfer mechanism of orthorhombic tungsten bronze β-$SrTa_2O_6:Eu^{3+}$ phosphor. RSC. Adv. 2023;13:12375. Available from: <DOI>.

13. Binnemans K. Interpretation of europium(III) spectra, Coord. Chem. Rev. 2015;295: 1–45. Available from: <DOI>.

14. Walrand CG, Binnemans K. *Handbook on the physics and chemistry of rare earths*, Elsevier, Belgium, 1998, pp.101–264.

15. Ekmekçi MK, İlhan M, Ege A, Ayvacıklı M. Microstructural and radioluminescence characteristics of Nd^{3+} doped columbite-type $SrNb_2O_6$ phosphor. J. Fluoresc. 2017;27:973–979. Available from: <DOI>.

16. Pullar RC. The Synthesis, Properties, and Applications of Columbite Niobates ($M^{2+}Nb_2O_6$): A Critical Review. J. Am. Ceram. Soc., 92;2009:563–577. Available from: <DOI>.

17. İlhan M, Ekmekçi MK, Oraltay RG, Başak AS. Structural and near-infrared properties of Nd^{3+} activated Lu_3NbO_7 Phosphor. J. Fluoresc. 2017;27:199–203. Available from: <DOI>.

18. İlhan M, Ekmekçi MK, Keskin İÇ. Judd–Ofelt parameters and X-ray irradiation results of $MNb_2O_6:Eu^{3+}$ (M = Sr, Cd, Ni) phosphors synthesized via a molten salt method. RSC Adv. 2021;11:10451. Available from: <DOI>.

19. Scharf W, Weitzel H, Yaeger I, Maartense I, Wanklyn BM. Magnetic structures of $CoNb_2O_6$. J. Magn. Magn. Mater. 1979;13:121-124. Available from: <DOI>.

20. Sarvezuk PWC, Kinast EJ, Colin CV, Gusmao MA, Cunha JBM da, Isnard O. New investigation of the magnetic structure of $CoNb_2O_6$ columbite. J. Appl. Phys. 2011;109: 07E160. Available from: <DOI>.

21. Xu Y, Wang LS, Huang YY, Ni JM, Zhao CC, Dai YF, Pan BY, Hong XC, Chauhan P, Koohpayeh SM, Armitage NP, and Li SY. Quantum critical magnetic excitations in spin-1/2 and Spin-1 chain systems. Physical Review X 2022;12:021020. Available from: <DOI>.

22. Lei S, Wang C, Guo D, Gao X, Cheng D, Zhou J, Cheng B, Xiao Y. Synthesis and magnetic properties of MNb_2O_6 (M = Fe, Co, Ni) nanoparticles. RSC Adv. 2014;4:52740. Available from: <DOI>.

23. Ringler JA, Kolesnikov AI, Ross KA. Single-ion properties of the transverse-field Ising model material $CoNb_2O_6$. Phys. Rev. B 2022;105:224421. Available from: <DOI>.

24. Zhang Y, Liu S, Zhang Y, Xiang M. Microwave dielectric properties of low-fired $CoNb_2O_6$ ceramics

with B_2O_3 addition. J Mater Sci: Mater Electron 2016;27:11293–11298. Available from: <DOI>.

25. Erdem R, İlhan M, Ekmekçi MK, Erdem Ö. Electrospinning, preparation and photoluminescence properties of $CoNb_2O_6$:Dy^{3+} incorporated polyamide 6 composite fibers. Appl. Surf. Sci. 2017;421:240-246. Available from: <DOI>.

26. Ekmekçi MK, İlhan M, Güleryüz LF, Mergen A. Study on molten salt synthesis, microstructural determination and white light emitting properties of $CoNb_2O_6$:Dy^{3+} phosphor. Optik. 2017;128:26–33. Available from: <DOI>.

27. Ekmekçi MK, Erdem M, Başak AS, Mergen A. Molten salt synthesis, visible and near-IR region spectral properties of europium or neodymium doped $CoNb_2O_6$ columbite niobate. Dalton Trans. 2015;44:5379. Available from: <DOI>.

28. Balamurugan C, Maheswari AH, Lee DW. Structural, optical and selective ethanol sensing properties of p-type semiconducting $CoNb_2O_6$ nano powder. Sens. Actuators B Chem. 2014;205:289-297. Available from: <DOI>.

29. Liu F, Wang B, Yang X, Guan Y, Sun R, Wang Q, Liang X, Sun P, Lu G. High-temperature stabilized zirconia-based sensors utilizing MNb_2O_6 (M: Co, Ni and Zn) sensing electrodes for detection of NO_2. Sens. Actuators B Chem. 2016;232:523–530. Available from: <DOI>.

30. Hanawa T, Shinkawa K, Ishikawa M, Miyatani K, Saito K, Kohn K. Anisotropic spesific heat of $CoNb_2O_6$ in magnetic fields. J. Phys. Soc. Japan 1994;63:2706-2715. Available from: <DOI>.

31. Liang T, Koohpayeh SM, Krizan JW, McQueen TM, Cava RJ, Ong NP. Heat capacity peak at the quantum critical point of the transverse Ising magnet $CoNb_2O_6$. Nat. Commun. 2015;6:7611. Available from: <DOI>.

32. Mulla IS, Natarajan N, Gaikwad AB, Samuel V, Guptha UN, Ravi V. A coprecipitation technique to prepare $CoTa_2O_6$ and $CoNb_2O_6$. Mater. Lett. 2007;61:2127–2129. Available from: <DOI>.

33. Felten EJ, Sprang PG, Rosen S. Phase Relations in the System $CoNb_2O_6$-$CoTa_2O_6$. J. Am. Ceram. 1966;49:273-276. Available from: <DOI>.

34. İlhan M, Keskin İÇ, Gültekin S. Assessing of photoluminescence and thermoluminescence properties of Dy^{3+} doped white light emitter TTB-lead metatantalate phosphor. J. Electron. Mater. 2020;49:2436-2449. Available from: <DOI>.

35. Saraf R, Shivakumara C, Behera S, Nagabhushana H, Dhananjaya N. Photoluminescence, photocatalysis and Judd-Ofelt analysis of Eu^{3+}-activated layered BiOCl phosphors. RSC Adv. 2015;5:4109–4120. Available from: <DOI>.

36. Blasse G. Energy transfer between inequivalent Eu^{2+} ions. Solid State Chem. 1986;62:207–211. Available from: <DOI>.

37. Blasse G. Energy transfer in oxidic phosphors. Philips Res. Rep. 1969;24:131-144.

38. Van Uitert LG. Characterization of energy transfer interactions between rare earth ions. J. Electrochem. Soc. 1967;114:1048–1053. Available from: <DOI>.

39. Judd BR. Optical Absorption Intensities of Rare-Earth Ions. Phys Rev. 1962;127:750. Available from: <DOI>.

40. Ofelt GS. Intensities of crystal spectra of rare-earth ions. J. Chem. Phys. 1962;37: 511. Available from: <DOI>.

41. İlhan M, Keskin İÇ. Analysis of Judd–Ofelt parameters and radioluminescence results of $SrNb_2O_6$:Dy^{3+} phosphors synthesized via molten salt method. Phys. Chem. Chem. Phys. 2020;22:19769. Available from: <DOI>.

42. Batsanov SS. *Structurnaya refractometria*, Moscow "Visshaya Shkola", 1976.

43. Shannon RD, Fischer RX. Empirical electronic polarizabilities in oxides, hydroxides, oxyfluorides, and oxychlorides. Phys. Rev. B. 2006;73:235111. Available from: <DOI>.

44. Bokii GB, Koshits MAP. *X-ray Structure Analysis*, MSU, Moscow, 1964.

45. Korotkov AS, Atuchin VV. Prediction of refractive index of inorganic compound by chemical formula. Opt. Commun. 2008;281:2132–2138. Available from: <DOI>.

46. İlhan M, Keskin İÇ. Evaluation of structural behaviour, radioluminescence, Judd-Ofelt analysis and thermoluminescence kinetic parameters of Eu^{3+} doped TTB–type lead metaniobate phosphor. Phys. B: Condens. Matter 2020;585:412106. Available from: <DOI>.

47. İlhan M, Güleryüz LF, Keskin İÇ, Katı Mİ. A comparison of spectroscopic properties of Dy^{3+}-doped tetragonal tungsten bronze MTa_2O_6 (M = Sr, Ba, Pb) phosphors based on Judd–Ofelt parameters.

Mater. Sci: Mater. Electron 2022;33:16606–16620. Available from: <DOI>.

48. Werts MHV, Jukes RTF, Verhoeven JW. The emission spectrum and the radiative lifetime of Eu^{3+} in luminescent lanthanide complexes. Phys. Chem. Chem. Phys., 2002;4:1542–1548. Available from: <DOI>.